Brooks Range Perennial Snowfields: Extent Detection from the Field and via Satellite - Supplemental Material

Molly E. Tedesche[1,2], Erin D. Trochim[3], Steven R. Fassnacht[4], and Gabriel J. Wolken[5,6]

[1]US Army Corps Engineer Research and Development Center, Cold Regions Research and Engineering Laboratory, Hanover, NH, USA, and Coastal and Hydraulics Laboratory, Vicksburg, MS, USA
[2]Water and Environmental Research Center, University of Alaska Fairbanks, Fairbanks, AK, USA
[3]Center for Energy and Power, University of Alaska Fairbanks, Fairbanks, AK, USA
[4]Department of Watershed Science, Colorado State University, Fort Collins, CO, USA
[5]Climate and Cryosphere Hazards Program, Alaska Division of Geological and Geophysical Surveys, Fairbanks, AK, USA
[6]Alaska Climate Adaptation Science Center, University of Alaska Fairbanks, Fairbanks, AK, USA

Correspondence: Molly E. Tedesche (metedesche@alaska.edu)

S1 Additional Background Information

Seasonal and perennial snow and ice cover are monitored using an array of various field-based techniques, as well as with remote sensing via aerial and satellite imagery. Some of the most widely utilized satellite imagery for mapping and tracking changes in the cryosphere include Land Remote-Sensing Satellite System (Landsat) (Markham et al., 2004; Li and Roy, 2017) and Moderate Resolution Imaging Spectroradiometer (MODIS) satellite imagery (Hall et al., 2002; Salomonson and Appel, 2004; Macander et al., 2015; Margulis et al., 2016), including changes in perennial snowfields (Tedesche et al., 2019). A relatively new collection of satellites being used to monitor snow and ice is the Copernicus Sentinel satellite constellation, which consists of multi-spectral imaging and synthetic aperture radar (SAR). Multiple studies have been conducted recently comparing the accuracy of mapping snow and ice using multi-spectral images from Sentinel and Landsat (Paul et al., 2016; Naegeli et al., 2017; Gascoin et al., 2019).

Often, studies involving automated mapping of snow and ice employ the Normalized Difference Snow Index (NDSI), which uses the green and short-wave infrared spectral bands to map snow cover extent (Dozier, 1989). NDSI is an effective method for mapping both seasonal (Salomonson and Appel, 2004; Macander et al., 2015) and perennial (Selkowitz and Forster, 2016a,b; Tedesche et al., 2019) snow and ice as a numerical indicator that highlights snow cover over land and uses the difference of these bands divided by their sum. While both clouds and snow reflect incident visible radiation, snow can be delineated from clouds because snow absorbs short-wave radiation and clouds do not (Tedesche et al., 2019).

NDSI is an effective method for distinguishing snow from clouds, however, it is still not perfect, and the two cannot be completely deciphered in all instances. Therefore, cloud masking is typically needed when analyzing multi-spectral imagery to find snow and ice cover (Stillinger et al., 2019). One effective cloud mask is the Fmask algorithm, which is used for the identification and removal of clouds and cloud shadows through a mosaicking process of images from Landsat missions 4–7 (Zhu and Woodcock, 2012). There is also a new version of Fmask for Landsat 8 and Sentinel-2 (Zhu et al., 2015).

Due to the challenges in discerning clouds from snow in multi-spectral remote sensing, some studies focus on the utility of SAR data via satellite as an alternative for snow detection (Tiuri et al., 1984; Nagler et al., 2016; Lievens et al., 2021). SAR operates independently from cloud cover, as radar backscatter can be measured through clouds, and changes in the radar signal over time have been used to find snow and ice cover (Mätzler, 1987; Shi and Dozier, 1995; Chang et al., 2014). Backscatter is the portion of the outgoing radar signal that the target redirects directly back towards the radar antenna. It is a measure of the reflective strength of a radar target. Other portions of the incident radar energy may be reflected and scattered away from the radar or absorbed. If the signal formed by backscatter is undesired, it is called clutter, however in remote sensing of the cryosphere, backscatter has become a useful tool (Rott and Mätzler, 1987; Bernier et al., 1999; Liang et al., 2021).

SAR change detection algorithms for wet snow, and wet snow/firn surfaces of the perennial snowfields in summer in the case of this study, work on the phenomenon that liquid water, which has a dielectric constant of 80.4 at a temperature of 20 °C, dramatically attenuates radar signals (Barker and Watts, 1973). The dielectric constant is the relative permittivity of a dielectric material, such as water. Liquid water creates high dielectric losses, and therefore reduces the backscatter coefficient ($\boldsymbol{\sigma^0}$) of wet snow and firn, compared to surfaces covered by dry snow (Evans, 1965; Tiuri et al., 1984). This means that in the winter composite image, the radar signal will pass right through dry snow and return a signal similar to that seen when the signal is returned from dry bare ground in the summer.

The backscatter coefficient ($\boldsymbol{\sigma^0}$) of snow decreases with increasing liquid water content (Shi and Dozier, 1995; Ulaby et al., 2014). SAR C-band has a nominal frequency range of 8 to 4 GHz (3.75 to 7.5 cm wavelength). C-band penetration depth through dry seasonal snow cover is about 20 m, but for snow with a liquid water content of 5% by volume or more, penetration depth is only 3 cm (Mätzler, 1987). For dry snow, Most SAR signals in the C-band return from the boundary between dry snow and the ground, but radar signals reflect and scatter at the surface of wet snow (Nagler et al., 2016). This study takes advantage of this contrast between wet and dry snow backscatter to develop the SAR change detection algorithm for finding perennial snowfields in the Brooks Range using the S1 SAR C-band data.

The backscatter coefficient ($\boldsymbol{\sigma^0}$) of wet snow and firn also changes with temperature fluctuations caused by the diurnal cycle, especially in the spring, which may affect the snow backscatter retrieval abilities of SAR change detection methods. Refreezing of the surface layer during a cold night, causes an increase in $\boldsymbol{\sigma^0}$ due to the high scattering characteristics of the frozen layer (Reber et al., 1987; Floricioiu and Rott, 2001). Essentially, ice does not attenuate the radar signal in the same way as wet snow due to the differences in dielectric properties. This results in a decrease in the contrast of snow versus snow-free surfaces. Backscatter theory and experimental data indicate that this effect is less prominent at C-band SAR than at other bands with shorter wavelengths, because there is less scattering efficiency and more infiltration through frozen layers (Nagler et al., 2016).

It is also important to consider incident angular dependence of backscatter and its influence over SAR change detection algorithm capability to discern perennial snowfield snow cover area (SCA). The backscatter contrast between melting snow and snow-free surfaces changes with the local incidence angle of the radar beam, which refers to the normal surface (Nagler et al., 2016). For co-polarized backscatter in the S1 VV band, $\boldsymbol{\sigma^0}$ contrast decreases significantly at low incidence angles because of a strong rise of the backscatter signal of wet snow (Mätzler, 1987; Strozzi et al., 1997). Cross-polarized backscatter in the S1 VH band has less dependence on low incidence angles, but the backscatter noise may not be workable at higher angles (Nagler et al., 2016). For these reasons, this study uses both polarizations in the change detection algorithm, and each are weighted differently depending on the local incident angle. Due to the dependency of interpreting backscatter on incident angles, employing change detection to map snow across mountainous terrain like the Brooks Range is very challenging (Rott and Mätzler, 1987), although not impossible given the development of effective radiometric terrain correction algorithms (Vollrath et al., 2020).

S2 Detailed Description of Sentinel Data

The Sentinel satellite constellation, created by the European Space Agency (ESA) within the frame of the Global Monitoring for Environment and Security (GMES) Space Component, is a series of next-generation Earth observation missions, developed on behalf of the joint ESA / European Commission initiative Copernicus. Each Sentinel mission focuses on a different aspect of Earth observation (*sentinel.esa.int/web/sentinel/missions*).

The Copernicus Sentinel-2 constellation has two polar-orbiting satellites (Sentinel-2A and Sentinel-2B) in the same sun-synchronous orbit, phased at 180° to each other (Li and Roy, 2017). Sentinel-2A was launched on 23 June 2015, while Sentinel-2B satellite was launched on 7 March 2017. The S2 payload has a wide swath width (290 km) and a revisit time of 10 days at the equator with one satellite, or 5 days considering both satellites, resulting in 2-3 days at mid-latitudes (*sentinel.esa.int/web/sentinel/missions/sentinel-2*) (***Figure S1***). For polar locations, like the Brooks Range, S2 revisit time is even more frequent, due to the curvature of the earth and the satellites' orbit pattern. The S2 Multispectral Instrument (MSI) measures the Earth's reflected radiance in 13 spectral bands from the visible infrared (VNIR), classical red, green, blue (RGB), and near-infrared (NIR), to the shortwave infrared (SWIR) (Drusch et al., 2012). There are just several spatial resolutions (pixel sizes) amongst the S2 bands, with most at the 10 m scale and SWIR at a 20 m scale. However, S2 band spectral resolution varies greatly (***Figure S1***). The S2 product used in this study is the Level-1C Top of Atmosphere (TOA) reflectance. The spectral resolutions of the various bands of S2 TOA (measured in bandwidths) range from 15 nm to 175 nm (Drusch et al., 2012), while the radiometric resolution (measured in wavelengths) ranges from 442 nm to 2202 nm (***Figure S1***).

The Copernicus Sentinel-1 mission also comprises a constellation of two polar-orbiting satellites (Sentinel-1A and Sentinel-1B) operating day and night performing C-band Synthetic Aperture Radar (SAR) imaging, enabling them to acquire imagery regardless of the weather. Sentinel-1A was launched on 3 April 2014, while Sentinel-1B satellite was launched on 25 April 2016 (Potin et al., 2016) (***Figure S1***). Like S2, the S1 satellites share the same sun-synchronous, near-polar, circular orbit plane, but with a 180° orbital phasing difference (Torres et al., 2012). The C-band imaging operates in four modes with different resolutions (down to 5 m) and coverage (up to 400 km) with dual polarization capability (*sentinel.esa.int/web/sentinel/missions/sentinel-1*). SAR wavelengths are not impeded by cloud cover or a lack of illumination and can collect data over a site during day or night under any cloud cover condition.

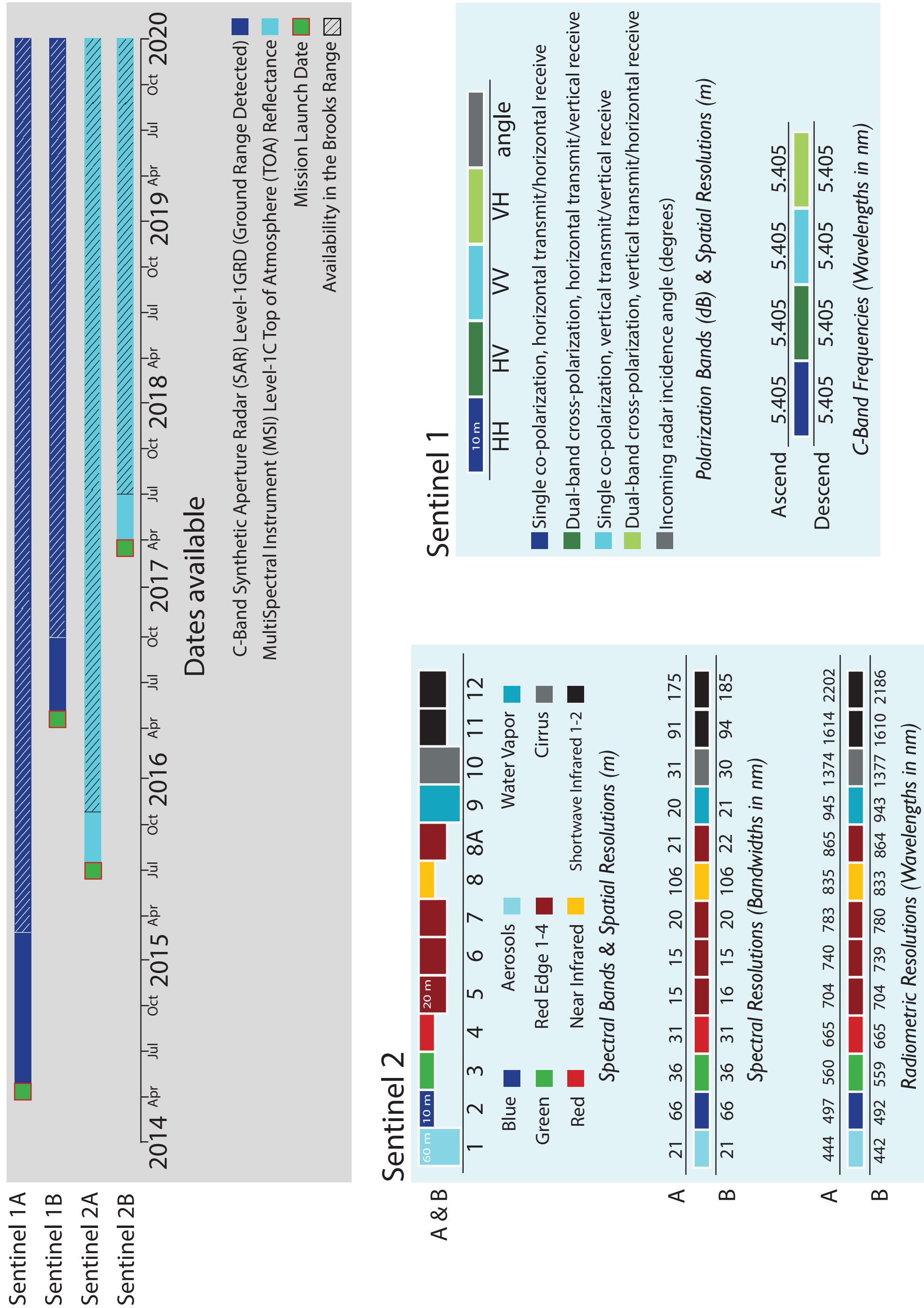

Figure S1. Sentinel-1 and 2 missions; years of data availability; optical and radar bands acquired; spatial, spectral, and radiometric resolutions.

S1 has a 12-day repeat cycle at the Equator with each pass being ascending or descending and the revisit rate is significantly greater over the Brooks Range and other polar locations. S1 operates in four exclusive acquisition modes: Stripmap (SM), Extra-Wide swath (EW), Wave (WV), and Interferometric Wide swath (IW) (Torres et al., 2012). IW is the mode used in the algorithm developed in this study. IW acquires data with a 250 km swath at 5 m by 20 m spatial resolution (single look) and incidence angles ranging from 29.1° to 46.0° (*sentinel.esa.int/web/sentinel/ missions/sentinel-1*) (***Figure S1***).

In this study, the S1 SAR product used is the Level-1 Ground Range Detected (GRD), which consists of focused SAR data that has been detected, multi-looked to reduce speckling, and projected to ground range using an Earth ellipsoid model (Torres et al., 2012, Potin et al., 2016). The resulting product has approximately square spatial resolution pixels and square pixel spacing with reduced speckle at the cost of worse spatial resolution. GRD products can be in one of three resolutions: Full Resolution (FR), High Resolution (HR), or Medium Resolution (MR). The resolution is dependent upon the amount of multi-looking performed. Level-1 GRD products are available in MR and HR for IW mode (*sentinel.esa.int/web/sentinel/missions/sentinel-1*). Each GRD scene contains either one or two out of four possible polarization bands, with possible combinations being single band VV or HH, and dual band VV+VH and HH+HV, where:

VV: *single co-polarization, vertical transmit/vertical receive*
HH: *single co-polarization, horizontal transmit/horizontal receive*
VV + VH: *dual-band cross-polarization, vertical transmit/horizontal receive*
HH + HV: *dual-band cross-polarization, horizontal transmit/vertical receive*

The Sentinel-1 C-band SAR instruments supports operation in single polarization (HH or VV) and in dual polarization (HH+HV or VV+VH) for the IW product (***Figure S1***). Each scene also includes an additional 'angle' band that contains the approximate instrument viewing angle in each pixel. Of the available polarization band combinations in IW, this study uses the VV single co-polarization and the VV + VH dual-band cross-polarization (herein referred to simply as VH), as these are the bands typically used in other SAR backscatter change detection algorithms for monitoring snow and ice (Nagler et al., 2016; Liang et al., 2021; Lievens et al., 2019 and 2021). Snow is a dense medium of clustered, irregularly shaped, ice crystals that contribute most strongly to radar backscattering in cross-polarized (VH) and co-polarized (VV) observations (Chang et al., 2014). Therefore, these previous studies make use of a ratio in linear scale (or difference in dB scale) between cross- and co-polarized backscatter to reduce impacts of non-snow surfaces and enhance snow sensitivity (Bernier et al., 1999; Lievens et al., 2019 and 2021).

S3 Extended Methods

S1 and S2 imagery were accessed and analyzed using Google Earth Engine (GEE), a cloud-computing platform for planetary scale geospatial analysis (Gorelick et al., 2017). GEE integrates a cloud-based computing environment co-located with satellite and climate reanalysis data. In this study, field acquired spatial datasets were uploaded and analyzed in GEE. All the remotely sensed datasets used in this study were fully archived with pixel-scale co-registration of all scenes in GEE and TOA reflectance for S2 are pre-calculated and calibrated (Gorelick et al., 2017). For S1 scenes in the Brooks Range, which is located above 60 degrees latitude, GEE also applies a terrain correction using the NASA Advanced Spaceborne Thermal Emission and Reflection Radiometer (ASTER) DEM. The final terrain-corrected values are converted to decibels via log scaling (10*log10(x)) by GEE. The ASTER DEM is only available at a coarse 60 m pixel scale in the study area, therefore, additional corrections were also manually applied using the better resolution, 10 m NASA ABoVE Composite DEM v2.1 (Burns et al., 2018).

One important pre-processing step for both S1 SAR backscatter change detection and for S2 NDSI is Simple Non-Iterative Clustering (SNIC), an image partitioning algorithm used to grow super pixels based on multiple bands. SNIC creates pixel clusters using imagery information such as texture, color, pixel values (digital numbers), shape, and size. This clustering process is a bottom-up, seed-based, segmentation approach that groups neighboring pixels together into clusters based on input data and parameters such as compactness, connectivity, and neighborhood size. The reason for applying SNIC to imagery before classifying land cover types (in this study, simply a binary of snow or no snow) is to create classified results with less of the "salt and pepper" effect of single outlier and/or misclassified pixels due to the complexity of an image.

Turning an image into small clusters of connected pixels, called "super pixels" is an effective pre-processing tool that simplifies an image from potentially millions of pixels to about two orders of magnitude fewer clusters of similar pixels (Achanta and Susstrunk, 2017). The SNIC image partitioning technique is typically applied to multi-spectral images like those in S2, where the clusters use characteristics found from multiple spectral bands; however, in this study, the SNIC technique was also a critical component of the S1 SAR change detection algorithm, where the clusters were based only on one band value, that of backscatter difference measured in dB.

During pre-processing, masking procedures were applied to increase efficiency by removing certain areas from consideration. This included areas with no snow cover in summer, such as surface water, low elevations, and extreme slope angles, as was done by Tedesche et al. (2019). Liquid water was detected in the S2 imagery using NDWI with a threshold value of 0.25, which is the ratio of the difference between the green spectral band and the near-infrared band over the sum of these bands. Since the S1 algorithm results are not spectral, liquid water was masked in S1 using the Global Surface Water Recurrence dataset (Pekel et al., 2016).

Areas that do not retain seasonal or perennial snow in summer also include low elevation valleys and extremely steep slope angles over 55°. These areas were masked out using the NASA ABoVE DEM. Aufeis occurring on valley river bottoms has a similar spectral signature as perennial snowfields and was also removed from consideration when the low elevation valleys were masked out. Lastly, larger glaciers located in the Arctic National Wildlife Refuge (ANWR) in the Eastern Brooks Range that are not perennial snow, were identified using the Global Land Ice Measurements from Space (GLIMS) layer in GEE (Cogley et al., 2015; GLIMS and NSIDC, 2018). This last step was only necessary at the end, when S1 methods were compared to S2 NDSI across the entire Brooks Range.

S3.1 Sentinel-2 NDSI Analysis

To perform terrain corrections and masking functions for S2 and S1, the 10m NASA ABoVE Composite DEM v2.1 (Burns et al., 2018) tiles that were needed for full coverage of the Brooks Range study area were obtained from the ABoVE group. These tiles were then stitched together and trimmed to the study area spatial extent using Environmental Systems Research Institute (ESRI) ArcGIS version 10.7 GIS software. This DEM was then manually ingested into the GEE Application Program Interface (API).

An S2 modular cloud masking algorithm for the TOA product was used in this study with 6 weeks of summer season (1 July to 15 August) imagery to create a single cloud-free image for each year in the study period (2016 through 2019). Rather than simply mosaicking specific cloud-free pixels from the various summer scenes, the cloud masking process employed multiple code modules in GEE to create a thorough, stepwise process for removing clouds and creating an RGB/IR (red, green, blue, infrared) image that was representative of each summer season during the study period. The S2 TOA cloud masking process implemented ***four modules***, including ***(1)*** mitigation of shadows, ***(2)*** mitigation of clouds, ***(3)*** a bidirectional reflection distribution function (BRDF), and ***(4)*** topographic correction, based on GEE code from Poortinga et al. (2019).

The first module, mitigation of shadows, uses a threshold score for cloud shadow masking that takes the sum of IR bands to include as shadows. It also calculates the radius of the number of pixels to contract (negative buffer) clouds and cloud shadows by, which is intended to eliminate smaller cloud patches that are likely errors. Next, the module calculates the radius of the number of pixels to dilate (buffer) clouds and cloud shadows by, which is intended to include edges of clouds and cloud shadows that are often missed. Finally, a function for finding dark outliers in a time series is applied (Housman et al., 2018).

The second module, mitigation of clouds, computes a cloud score per pixel, and adds a band that represents the cloud mask. This cloud-masking algorithm for S2 is similar to the Landsat cloud score algorithm employed by Irish et al. (2006) and Tedesche et al. (2019). The data were first cloud-masked using a simple and standardized approach to arrive at a cloud score per pixel (Irish et al., 2006). To verify that clouds were not snow, the cloud score also included an NDSI calculation and then a derived image of cloud scores corresponding to each pixel was created to screen out excessively cloudy pixels. Also, the quality band (QA60) for S2 was used to exclude pixels designated as "cirrus" or "cloud."

The BRDF module accounts for the fact that the derived surface reflectance in S2 is generally directional, and as such, depends upon the incident solar and receiving detector angles. The BRDF module is used to compensate for the anisotropic reflectance of a material (such as clouds) and employs a nadir BRDF-adjusted reflectance (NBAR) and fixed spectral parameters (Roy et al., 2017). The fourth cloud masking module, topographic illumination correction, uses terrain layers from the DEM (slope and aspect) within a function to calculate the illumination condition using solar position. This illumination condition is then corrected to lessen effects on the image being cloud masked.

Finally, a composite was made using the median TOA reflectance value from all non-cloud covered pixels available per summer for each pixel. This technique also provides additional mitigation of the darkening effects of mountain shadows and cloud shadows. The composite images were then processed through the SNIC image partitioning and the masking processes. A percentile function was applied where the darkest 25% of each pixel in the snowfield was removed from the bottom 75th percentile (darkest 75% of each pixel). The last step was to apply NDSI to each processed cloud-free mosaic to determine perennial snowfield SCA, using an NDSI value threshold range between 0.4 and 1.0, with 0.4 being a widely accepted value derived from the literature (Dozier, 1989) and 1.0 being an empirically derived value found for this study through an iterative process.

S3.2 Sentinel-1 SAR Backscatter Change Detection Algorithm

The SAR change detection algorithm is minimally influenced by diurnal variations in radar backscatter due to very low amplitude diurnal temperature variations at this high northern latitude (67-69° N) study area. The Brooks Range receives extreme amounts of daylight and darkness near the summer and winter solstices, respectively, and there is little change in daily temperature during the seasons from which the summer S1 and winter reference S1 scenes are taken. In the mid-winter, the Brooks Range receives almost no sunlight and temperatures stay below freezing all day, while in the mid-summer, this is reversed, with temperatures rarely below freezing.

Exceptions to this in summer may include a snowfield refreezing cycle in late August as darkness is returning, on north-facing aspects that hold perennial snowfields, especially if the terrain above has extreme slope angles that put the snowfields into shadow for part of each day. This is in fact, one of the formational causes and persistence mechanisms of perennial snowfields. For this study's location and period (2016 to 2019), the S1 satellites typically passed over for scene acquisition during either the 15:00 and 16:00 UTC hours (6am to 7am in Alaska), or during the 02:00 to 03:00 UTC hours (5pm to 6pm in Alaska). Upon detailed manual inspection of summer S1 scenes input into the SAR change detection algorithm in this polar region, there was little to no evidence of variation in $\boldsymbol{\sigma^0}$ values in images taken at various times of day.

To develop the SAR change detection algorithm, the backscatter values in each pixel of a single S1 scene manually selected from the summer study period of 1 July through 15 August were differenced from those at the same location during the previous winter. Here, summer season is defined in this study as the time of snowfield minimum extent (late summer) when perennial layers are revealed beneath the seasonal snow cover. When possible, the single S1 summer image was chosen closest to the middle of the season, around 20 to 25 July. Due to the location and orientation of the S1 swaths, it was frequently necessary to choose two to four images around this time frame and mosaic them to encompass the entire AKP study area (***Figure S2***). The previous winter reference image was derived using a composite of ascending and descending orbit scenes from S1 during the month of January from the same year as the summer single scene. This composite was created by taking the focal median to remove or lessen the effect of speckling in the SAR imagery.

After the S1 SAR winter reference composite and single summer images were chosen, an angular-based radiometric slope correction was applied (Vollrath et al., 2020). This slope correction was employed to lessen the effects of surface scattering on the backscatter signal, which is a significant issue in mountainous and complex terrain, such as that of the Brooks Range. Radiometric distortions over rugged terrain within SAR backscatter products originate from the side-looking SAR imaging geometry and are strong enough to exceed weaker differences of the signal due to variation in land cover (Small, 2011). S1 SAR imagery from GEE's GRD collection are pre-processed by applying an orbit file, removing thermal and border noise, applying a radiometric calibration to $\boldsymbol{\sigma^0}$, and applying a range-doppler correction (Vollrath et al., 2020).

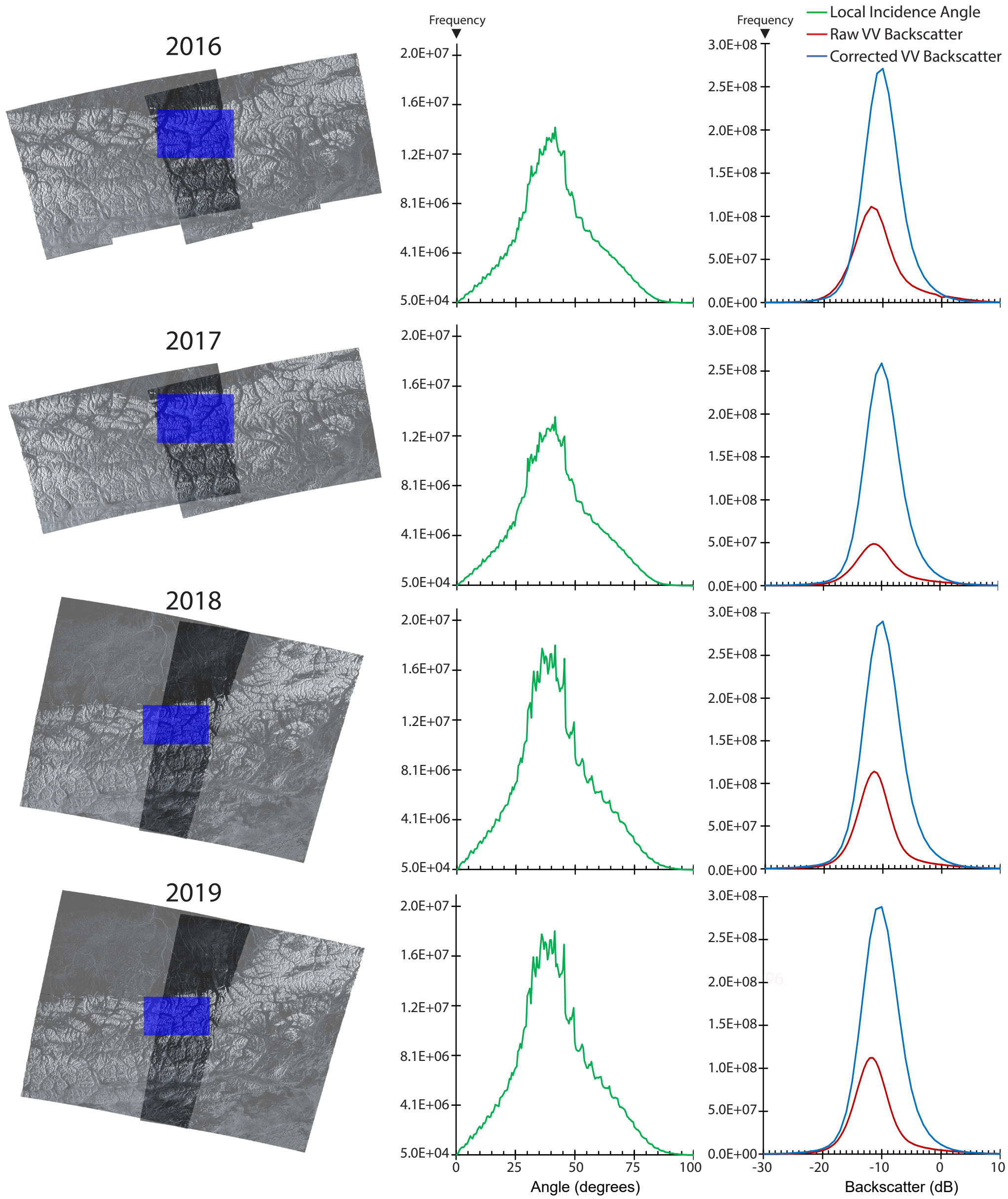

Figure S2. S1 SAR raw swaths and band values used to create images for each summer during the period of 2016 – 2019 in the AKP study area. ***Left column:*** Swath locations and location of the AKP study area (in blue). Summer backscatter ratios were calculated with winter composite image backscatter. ***Middle column:*** Frequency histograms of SAR backscatter incidence angles calculated for each 10 m x 10 m pixel in corresponding raw SAR swaths. ***Right column:*** Frequency histograms of backscatter values (dB) in each pixel in the corresponding raw SAR swaths, before and after angular-based radiometric slope correction.

However, GEE does not apply a final radiometric slope correction, as DEM availability varies globally. Therefore, the final radiometric slope correction, for this study area in the Brooks Range, was calculated and applied manually using the angular relationships between the SAR image and the terrain geometry derived from the ABoVE 10 m DEM (***Figure S2***). This included simplified relationships between four angles, including radar nominal (incidence) angle, radar look direction, terrain slope steepness, and terrain slope aspect angle (Vollrath et al., 2020) (***Figure S2***). The radiometric slope correction also generates masks of invalid data in active layover and shadow affected areas. The local incidence angle was calculated using the trigonometric relationship between terrain slope, terrain angle, and incoming angle of the SAR radar signal (***Figure S2***).

During the development of the SAR change detection algorithm, the VV backscatter difference had a much stronger contrast than that of VH, so the VV portion of the algorithm was weighted by a factor of 3. This factor was found after many iterations of trial and error to be the most effective weighting constant for discerning perennial snowfields from bare ground in the resultant images created using the SAR change detection algorithm. Resultant images of combined VV and VH ratios were thresholded using a binary Otsu approach (Lv et al., 2020) to find a dynamic value unique to each image that delineated the perennial snowfields in summer.

S3.3 Field Evaluations

For 2016 and 2017, S1 and S2 results are compared to the field acquired helicopter point data from 2015 using the Cohen's Kappa coefficient (***K***). Percent accuracies (***% A***) were also calculated for the four datasets: S1 2016, S1 2017, S2 2016, and S2 2017, as the number of times a snowfield was observed in the Sentinel data as co-located under a helicopter point (***Sn***), divided by the total number of helicopter points (***Hn = 189***). Cohen's Kappa coefficient is a statistic used to measure inter-rater reliability (and also intra-rater reliability) for qualitative (categorical; yes or no) items. It is generally thought to be a more robust measure than simple percent agreement calculation, as ***K*** takes into account the possibility of the agreement occurring by chance (McHugh, 2012). Cohen's Kappa, as it relates to this study, was calculated as:

		S1	
		Yes	*No*
S2	*Yes*	a	b
	No	c	d

Where **S1** is the result of the Sentinel-1 SAR change detection algorithm, **S2** is the result of the Sentinel-2 optical/multi-spectral NDSI analysis, *Yes* is when a snowfield is observed in the Sentinel results under a helicopter point, and *No* is when a snowfield is *not* observed in the Sentinel results under a helicopter point. ***K*** is defined as:

$$K = \frac{P_o - P_e}{1 - P_e} \qquad \text{Eqn. (S1)}$$

where:

$$P_o = \frac{a + d}{a + b + c + d} \qquad \text{Eqn. (S2)}$$

$$P_{yes} = \frac{a + b}{a + b + c + d} * \frac{a + c}{a + b + c + d} \qquad \text{Eqn. (S3)}$$

$$P_{no} = \frac{c + d}{a + b + c + d} * \frac{b + d}{a + b + c + d} \qquad \text{Eqn. (S4)}$$

$$P_e = P_{yes} + P_{no} \qquad \text{Eqn. (S5)}$$

References

Achanta, R. and Susstrunk, S.: Superpixels and Polygons Using Simple Non-iterative Clustering, in: 2017 IEEE Conference on Computer Vision and Pattern Recognition (CVPR), 2017 IEEE Conference on Computer Vision and Pattern Recognition (CVPR), Honolulu, HI, 4895–4904, https://doi.org/10.1109/CVPR.2017.520, 2017.

Barker, J. A. and Watts, R. O.: Monte Carlo studies of the dielectric properties of water-like models, Molecular Physics, 26, 789–792, 1973.

Bernier, M., Fortin, J.-P., Gauthier, Y., Gauthier, R., Roy, R., and Vincent, P.: Determination of snow water equivalent using RADARSAT SAR data in eastern Canada, Hydrol. Process., 13, 3041–3051, https://doi.org/10.1002/(SICI)1099-1085(19991230)13:18<3041::AID-HYP14>3.0.CO;2-E, 1999.

Burns, P. J., Massey, R., and Goetz, S. J.: NASA ABoVE 10m Composite DEM, 2018, G54A-05, 2018.

Chang, W., Tan, S., Lemmetyinen, J., Tsang, L., Xu, X., and Yueh, S. H.: Dense Media Radiative Transfer Applied to SnowScat and SnowSAR, IEEE J. Sel. Top. Appl. Earth Observations Remote Sensing, 7, 3811–3825, https://doi.org/10.1109/JSTARS.2014.2343519, 2014.

Cogley, G. (submitter); Kienholz, C., Miles, E., Sharp, M., and Wyatt, F. (analyst(s)): GLIMS Glacier Database. Boulder, CO. National Snow and Ice Data Center, http://dx.doi.org/10.7265/N5V98602, 2015

Dozier, J.: Spectral signature of alpine snow cover from the Landsat Thematic Mapper, Remote sensing of environment, 28, 9–22, 1989.

Drusch, M., Del Bello, U., Carlier, S., Colin, O., Fernandez, V., Gascon, F., Hoersch, B., Isola, C., Laberinti, P., Martimort, P., Meygret, A., Spoto, F., Sy, O., Marchese, F., and Bargellini, P.: Sentinel-2: ESA's Optical High-Resolution Mission for GMES Operational Services, Remote Sensing of Environment, 120, 25–36, https://doi.org/10.1016/j.rse.2011.11.026, 2012.

Evans, S.: Dielectric properties of ice and snow–a review, Journal of Glaciology, 5, 773–792, 1965.

Floricioiu, D. and Rott, H.: Seasonal and short-term variability of multifrequency, polarimetric radar backscatter of Alpine terrain from SIR-C/X-SAR and AIRSAR data, IEEE Transactions on Geoscience and Remote Sensing, 39, 2634–2648, https://doi.org/10.1109/36.974998, 2001.

Gascoin, S., Grizonnet, M., Bouchet, M., Salgues, G., and Hagolle, O.: Theia Snow collection: high-resolution operational snow cover maps from Sentinel-2 and Landsat-8 data, 22, 2019.

GLIMS and NSIDC: Global Land Ice Measurements from Space glacier database. Compiled and made available by the international GLIMS community and the National Snow and Ice Data Center, Boulder CO, U.S.A. https://doi.org/10.7265/N5V98602, 2018.

Gorelick, N., Hancher, M., Dixon, M., Ilyushchenko, S., Thau, D., and Moore, R.: Google Earth Engine: Planetary-scale geospatial analysis for everyone, Remote Sensing of Environment, 202, 18–27, https://doi.org/10.1016/j.rse.2017.06.031, 2017.

Hall, D. K., Riggs, G. A., Salomonson, V. V., DiGirolamo, N. E., and Bayr, K. J.: MODIS snow-cover products, Remote Sensing of Environment, 83, 181–194, https://doi.org/10.1016/S0034-4257(02)00095-0, 2002.

Housman, I. W., Chastain, R. A., and Finco, M. V.: An Evaluation of Forest Health Insect and Disease Survey Data and Satellite-Based Remote Sensing Forest Change Detection Methods: Case Studies in the United States, Remote Sensing, 10, 1184, https://doi.org/10.3390/rs10081184, 2018.

Irish, R. R., Barker, J. L., Goward, S. N., and Arvidson, T.: Characterization of the Landsat-7 ETM+ automated cloud-cover assessment (ACCA) algorithm, Photogrammetric engineering and remote sensing, 10, 1179-1188, 2006.

Li, J. and Roy, D.: A Global Analysis of Sentinel-2A, Sentinel-2B and Landsat-8 Data Revisit Intervals and Implications for Terrestrial Monitoring, Remote Sensing, 9, 902, https://doi.org/10.3390/rs9090902, 2017.

Liang, D., Guo, H., Zhang, L., Cheng, Y., Zhu, Q., and Liu, X.: Time-series snowmelt detection over the Antarctic using Sentinel-1 SAR images on Google Earth Engine, Remote Sensing of Environment, 256, 112318, https://doi.org/10.1016/j.rse.2021.112318, 2021.

Lievens, H., Brangers, I., Marshall, H.-P., Jonas, T., Olefs, M., and De Lannoy, G.: Sentinel-1 snow depth retrieval at sub-kilometer resolution over theEuropean Alps, Snow/Remote Sensing, https://doi.org/10.5194/tc-2021-74, 2021.

Lievens, H., Demuzere, M., Marshall, H.-P., Reichle, R. H., Brucker, L., Brangers, I., de Rosnay, P., Dumont, M., Girotto, M., Immerzeel, W. W., Jonas, T., Kim, E. J., Koch, I., Marty, C., Saloranta, T., Schöber, J., and De Lannoy, G. J. M.: Snow depth variability in the Northern Hemisphere mountains observed from space, Nat Commun, 10, 4629, https://doi.org/10.1038/s41467-019-12566-y, 2019.

Lv, Z., Liu, T., and Benediktsson, J. A.: Object-Oriented Key Point Vector Distance for Binary Land Cover Change Detection Using VHR Remote Sensing Images, IEEE Transactions on Geoscience and Remote Sensing, 58, 6524–6533, https://doi.org/10.1109/TGRS.2020.2977248, 2020.

Macander, M. J., Swingley, C. S., Joly, K., and Raynolds, M. K.: Landsat-based snow persistence map for northwest Alaska, Remote Sensing of Environment, 163, 23–31, https://doi.org/10.1016/j.rse.2015.02.028, 2015.

Margulis, S. A., Cortés, G., Girotto, M., and Durand, M.: A Landsat-Era Sierra Nevada Snow Reanalysis (1985–2015), Journal of Hydrometeorology, 17, 1203–1221, https://doi.org/10.1175/JHM-D-15-0177.1, 2016.

Markham, B. L., Storey, J. C., Williams, D. L., and Irons, J. R.: Landsat sensor performance: history and current status, IEEE Transactions on Geoscience and Remote Sensing, 42, 2691–2694, https://doi.org/10.1109/TGRS.2004.840720, 2004.

Mätzler, C.: Applications of the interaction of microwaves with the natural snow cover, Remote Sensing Reviews, 2, 259–387, https://doi.org/10.1080/02757258709532086, 1987.

McHugh, M. L.: Interrater reliability: the kappa statistic, Biochemia Medica, 22, 276–282, 2012.

Naegeli, K., Damm, A., Huss, M., Wulf, H., Schaepman, M., and Hoelzle, M.: Cross-Comparison of Albedo Products for Glacier Surfaces Derived from Airborne and Satellite (Sentinel-2 and Landsat 8) Optical Data, Remote Sensing, 9, 110, https://doi.org/10.3390/rs9020110, 2017.

Nagler, T., Rott, H., Ripper, E., Bippus, G., and Hetzenecker, M.: Advancements for Snowmelt Monitoring by Means of Sentinel-1 SAR, Remote Sensing, 8, 348, https://doi.org/10.3390/rs8040348, 2016.

Paul, F., Winsvold, S., Kääb, A., Nagler, T., and Schwaizer, G.: Glacier Remote Sensing Using Sentinel-2. Part II: Mapping Glacier Extents and Surface Facies, and Comparison to Landsat 8, Remote Sensing, 8, 575, https://doi.org/10.3390/rs8070575, 2016.

Pekel, J.-F., Cottam, A., Gorelick, N., and Belward, A. S.: High-resolution mapping of global surface water and its long-term changes, Nature, 540, 418–422, https://doi.org/10.1038/nature20584, 2016.

Poortinga, A., Tenneson, K., Shapiro, A., Nquyen, Q., San Aung, K., Chishtie, F., and Saah, D.: Mapping Plantations in Myanmar by Fusing Landsat-8, Sentinel-2 and Sentinel-1 Data along with Systematic Error Quantification, Remote Sensing, 11, 831, https://doi.org/10.3390/rs11070831, 2019.

Potin, M. P., Rosich, M. B., Grimont, M. P., Miranda, M. N., Shurmer, M. I., O'Connell, M. A., Torres, M. R., and Krassenburg, M. M.: Sentinel-1 Mission Status, 6, 2016.

Reber, B., Mätzler, C., and Schanda, E.: Microwave signatures of snow crusts Modelling and measurements, International Journal of Remote Sensing, 8, 1649–1665, https://doi.org/10.1080/01431168708954805, 1987.

Rott, H. and Mätzler, C.: Possibilities and Limits of Synthetic Aperture Radar for Snow and Glacier Surveying, Annals of Glaciology, 9, 195–199, https://doi.org/10.3189/S0260305500000604, 1987.

Roy, D. P., Li, J., Zhang, H. K., Yan, L., Huang, H., and Li, Z.: Examination of Sentinel-2A multi-spectral instrument (MSI) reflectance anisotropy and the suitability of a general method to normalize MSI reflectance to nadir BRDF adjusted reflectance, Remote Sensing of Environment, 199, 25–38, https://doi.org/10.1016/j.rse.2017.06.019, 2017.

Salomonson, V. V. and Appel, I.: Estimating fractional snow cover from MODIS using the normalized difference snow index, Remote Sensing of Environment, 89, 351–360, https://doi.org/10.1016/j.rse.2003.10.016, 2004.

Selkowitz, D. J. and Forster, R. R.: An Automated Approach for Mapping Persistent Ice and Snow Cover over High Latitude Regions, Remote Sensing, 8, 16, https://doi.org/10.3390/rs8010016, 2016a.

Selkowitz, D. J. and Forster, R. R.: Automated mapping of persistent ice and snow cover across the western U.S. with Landsat, ISPRS Journal of Photogrammetry and Remote Sensing, 117, 126–140, https://doi.org/10.1016/j.isprsjprs.2016.04.001, 2016b.

Shi, J. and Dozier, J.: Inferring snow wetness using C-band data from SIR-C's polarimetric synthetic aperture radar, IEEE Transactions on Geoscience and Remote Sensing, 33, 905–914, https://doi.org/10.1109/36.406676, 1995.

Small, D.: Flattening Gamma: Radiometric Terrain Correction for SAR Imagery, IEEE Trans. Geosci. Remote Sensing, 49, 3081–3093, https://doi.org/10.1109/TGRS.2011.2120616, 2011.

Stillinger, T., Roberts, D. A., Collar, N. M., and Dozier, J.: Cloud Masking for Landsat 8 and MODIS Terra Over Snow-Covered Terrain: Error Analysis and Spectral Similarity Between Snow and Cloud, Water Resour. Res., 55, 6169–6184, https://doi.org/10.1029/2019WR024932, 2019.

Strozzi, T., Wiesmann, A., and Mätzler, C.: Active microwave signatures of snow covers at 5.3 and 35 GHz, Radio Science, 32, 479–495, https://doi.org/10.1029/96RS03777, 1997.

Tedesche, M. E., Trochim, E. D., Fassnacht, S. R., and Wolken, G. J.: Extent Changes in the Perennial Snowfields of Gates of the Arctic National Park and Preserve, Alaska, Hydrology, 6, 53, https://doi.org/10.3390/hydrology6020053, 2019.

Tiuri, M., Sihvola, A., Nyfors, E., and Hallikaiken, M.: The complex dielectric constant of snow at microwave frequencies, IEEE J. Oceanic Eng., 9, 377–382, https://doi.org/10.1109/JOE.1984.1145645, 1984.

Torres, R., Snoeij, P., Geudtner, D., Bibby, D., Davidson, M., Attema, E., Potin, P., Rommen, B., Floury, N., Brown, M., Traver, I. N., Deghaye, P., Duesmann, B., Rosich, B., Miranda, N., Bruno, C., L'Abbate, M., Croci, R., Pietropaolo, A., Huchler, M., and Rostan, F.: GMES Sentinel-1 mission, Remote Sensing of Environment, 120, 9–24, https://doi.org/10.1016/j.rse.2011.05.028, 2012.

Ulaby, F.T., Long, D.G., Blackwell, W.J., Elachi, C., Fung, A.K., Ruf, C., Sarabandi, K., Zebker, H.A. and Van Zyl, J.: Microwave radar and radiometric remote sensing, Ann Arbor: University of Michigan Press, 4, 6, 2014.

Vollrath, A., Mullissa, A., and Reiche, J.: Angular-Based Radiometric Slope Correction for Sentinel-1 on Google Earth Engine, Remote Sensing, 12, 1867, https://doi.org/10.3390/rs12111867, 2020.

Zhu, Z. and Woodcock, C. E.: Object-based cloud and cloud shadow detection in Landsat imagery, Remote Sensing of Environment, 118, 83–94, https://doi.org/10.1016/j.rse.2011.10.028, 2012.

Zhu, Z., Wang, S., and Woodcock, C. E.: Improvement and expansion of the Fmask algorithm: cloud, cloud shadow, and snow detection for Landsats 4–7, 8, and Sentinel 2 images, Remote Sensing of Environment, 159, 269–277, https://doi.org/10.1016/j.rse.2014.12.014, 2015.